Probing the structures of bimetallic Sn/Rh(111) surfaces: Alkali-ion scattering and x-ray photoelectron diffraction studies

Yingdong Li, Michael R. Voss, Nathan Swami, Yi-Li Tsai, and Bruce E. Koel
Department of Chemistry, University of Southern California, Los Angeles, California 90089-0482
(Received 10 February 1997; revised manuscript received 14 July 1997)

We have investigated the bimetallic Sn/Rh(111) system formed by vapor deposition of Sn on a Rh(111) single-crystal surface by applying two powerful structural probes: alkali-ion scattering spectroscopy (ALISS) and x-ray photoelectron diffraction. For initial submonolayer exposures, the surface structure responsible for the observed $(\sqrt{3}\times\sqrt{3})R30°$-Sn/Rh(111) low-energy electron diffraction pattern is explored and its alloy nature is established. The Na^+ ALISS results indicate that the formation of this surface alloy is produced by the replacement of top-layer Rh atoms by Sn atoms. The resultant alloy surface can be strictly two dimensional if the annealing temperature is high enough ($\geqslant$1300 K). This surface alloy is buckled with the Sn atoms displaced upward from the Rh surface plane by 0.29 ± 0.05 Å. In addition, x-ray photoemission spectroscopy core-level measurements have been performed on this surface alloy at grazing exit angles and these are compared with results on the analogous Sn/Pt(111) surface alloy. Binding energy shifts of -0.4 and -0.6 eV for the Rh $3d$ and Sn $3d$ core levels, respectively, were observed for the Rh-Sn alloy compared to the pure elements. A shift of -0.3 eV was also seen for the valence-band centroid upon alloying. From temperature-programmed desorption studies it was determined that CO adsorption is decreased on the Sn/Rh surface alloy, but with only a small (4 kcal/mol) decrease in the adsorption energy. The growth mechanism of the Sn film in the Sn/Rh(111) bimetallic system was also probed. The vapor deposition of Sn on Rh(111) at 300 K does not form epitaxial clean Sn films or pure Sn clusters but rather forms a random alloy of increasing thickness. [S0163-1829(97)07440-7]

I. INTRODUCTION

The preparation of bimetallic compound or alloy surfaces is typically accomplished by either metal-vapor deposition followed by annealing to high temperatures or by cutting bulk metal alloys along a certain direction. Advantages of the first approach include the flexibility and control of the surface structure and composition. The challenges for this method are (1) establishing the final surface structure as an alloy surface as opposed to an overlayer, (2) determining the stoichiometry of the surface metal components, (3) identifying the alloy surface generated in such a manner as either two dimensional or ''bulklike'' and (4) discerning the flatness of the alloy surface that is driven by the redistribution of electronic charge at the surface. Answers to these issues are themselves very interesting since they involve a consideration of phase transitions and the nature of atom-atom interactions. Perhaps as importantly, they pave the way for a variety of chemical studies to be conducted on these well-defined bimetallic surfaces. One example is the chemisorption and reactions of NO on Sn/Rh alloy surfaces, which would be relevant to research on NO catalysis on supported Sn/Rh catalysts.[1] Rh is an active catalyst for reducing NO to N_2 and it is of interest to discern the effect this Sn-modified alloy surface has on NO adsorption and dissociation. Reactivity studies such as these are the driving force behind our detailed structural work on the Sn/Rh(111) bimetallic system. We address all of the structural issues described above explicitly in this paper.

The strength of low-energy alkali-ion scattering spectroscopy (ALISS) as a structural probe lies in its simplicity and accuracy in determining atom positions and its extreme surface sensitivity.[2] In the past few years this technique has been applied successfully to study various bimetallic systems such as Sn/Pt(111),[3] Sn/Ni(111),[4] Sn/Cu(111),[5] Sn/Ni(100),[6] and Sn/Pt(100),[7] among many others. It is convenient to apply this technique to ordered surfaces since the angle-dependent features in the spectra correlate directly to the periodicity of the atom spacing. By combining x-ray photoelectron diffraction[8,9] (XPD) with ALISS, we can obtain independent verification and also complimentary information on surface structures.[10] For example, the XPD technique has unique capabilities for determining the orientation of adsorbed molecules and metal growth morphology that ALISS lacks. We combine these two powerful structural probes in the same ultrahigh vacuum (UHV) chamber in order to carry out geometric structural determinations of bimetallic and alloy surfaces. In this paper, we describe our combined ALISS and XPD studies of the structures of bimetallic Sn/Rh(111) surfaces formed by vapor depositing Sn on the Rh(111) surface. In addition, we report on detailed x-ray photoemission spectroscopy (XPS) measurements and a preliminary CO temperature programmed desorption (TPD) study on a Sn/Rh(111) surface alloy that can be formed.

II. EXPERIMENTAL METHODS

The experimental arrangement and conditions were essentially the same as described previously.[6,7] The apparatus, as shown in Fig. 1, is a two-level UHV chamber with four-grid low-energy electron diffraction (LEED) optics that also serve as a retarding field analyzer (RFA) for Auger electron spectroscopy (AES) and has capabilities for gas dosing, metal

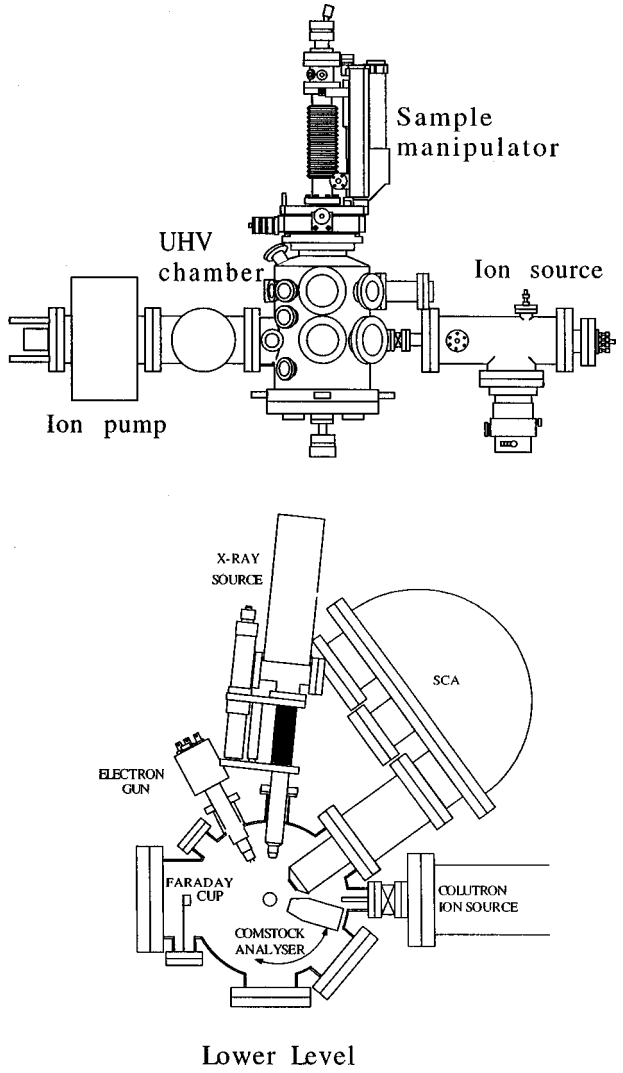

FIG. 1. Two-level UHV chamber for combined ALISS and XPD experiments.

evaporation, ion sputtering, and TPD at the top level. The bottom level contains a Colutron ion gun for ion scattering spectroscopy (ISS), a dual-anode x-ray source, and two electrostatic energy analyzers. A small Comstock electrostatic analyzer is mounted on a rotatable turntable inside the UHV chamber that allows the total scattering angle in ISS to be changed and the incident ion beam to be measured directly. The spectra shown herein were obtained primarily using a Perkin-Elmer Model 10-360 spherical capacitor analyzer (SCA) that is mounted on a fixed flange so that the scattering angle is always 144°. This analyzer is equipped with a multichannel detector with 16 discreet multipliers to provide high count rates. For the XPS studies, we operated the SCA with a 46.95-eV pass energy ($R=0.6$ eV and $\Delta E/E=0.5\%$) and utilized a Mg anode operated at 400 W. To enhance the surface sensitivity, we used an analysis angle for XPS that was 70° from the surface normal.

The sample stage holding the Rh(111) crystal can be rotated both on a polar plane ($\pm 180°$) and on a azimuthal plane ($\pm 90°$) and both of these rotations are controlled by stepping motors interfaced through a computer. The data acquisition routines for both ALISS and XPD are highly automated. The ion source used in this study was a sodium source from Spectra Mat Inc. The higher mass of Na^+ compared to that of Li^+ gave us better energy resolution, which was needed because of the small mass difference between Rh and Sn.

The Rh(111) single-crystal sample was $10\times10\times1$ mm^3 in size and oriented to within 0.5°. It was held onto the sample holder by two 0.5-mm Ta wires and could be cooled down to 200 K or electron-beam heated to 1500 K. Maintenance of the sample alignment is very important and therefore was accomplished carefully. The sample was first annealed to 1300 K in several cycles in vacuum to stabilize its position, and this was followed with an alignment procedure using a He-Ne laser beam mounted coaxially at the end of the Colutron ion source. This calibration procedure reduces the uncertainty of the polar and azimuthal angles to $<0.5°$ and $<1°$, respectively.

The crystal was cleaned by repeated cycles of Ar^+-ion sputtering (1 kV at 1000 K) and annealing in vacuum to 1300 K. The surface composition of the sample was checked by AES. LEED showed the expected $p(1\times1)$ pattern for the clean Rh(111) surface. The Sn doses were made by using an enclosed boat made from 0.13-mm Ta foil containing a Sn ingot (6*N* purity). This doser was thoroughly outgassed before use. The Sn deposition rate utilized with this doser was about 0.8 ML/min with a background pressure below 2×10^{-10} Torr.

The experimental apparatus used for the CO adsorption studies has been previously described.[11] The instrument is a three-level UHV chamber with a double-pass cylindrical mirror analyzer (CMA) on the top level, LEED and quadrupole mass spectrometer for TPD in the middle level, and a high-resolution electron-energy-loss spectroscopy (HREELS) spectrometer on the bottom level. The base pressure of the chamber was below 2×10^{-10} Torr. A different Rh(111) single crystal was used in these studies, which was 10 mm diameter$\times$1 mm thick and was mounted to a sample holder by 0.020-in. Ta wires. The sample could be cooled to 100 K or resistively heated to 1350 K. Sample cleanliness was achieved by Ar^+-ion sputtering and annealing as described above and verified by AES and LEED. Sn dosing was carried out by resistive evaporative heating in a manner identical to that in the ISS and XPD experiments. CO dosing was performed with a Varian leak valve. The TPD spectra obtained on this chamber were cross referenced to poorer quality spectra taken under similar conditions on the aforementioned ISS chamber. The CO desorption peak temperatures agreed well.

III. RESULTS

A. Sn deposition on Rh(111): AES and LEED studies

The results from AES and LEED are discussed first since they help characterize the surface composition and the long-range order and symmetry. Shown in Fig. 2 is a Sn uptake plot constructed from AES data obtained by the RFA in the ALISS chamber ($E_i=2$ keV and $V_{\rm mod}=10\,V_{pp}$), in which the AES intensities from Rh and Sn are plotted as a function of the Sn deposition time. The deposition was carried out with the Rh crystal at room temperature. From Fig. 2 it is seen that the Sn growth can be described initially by two linear regions of both the Sn and Rh AES intensities below

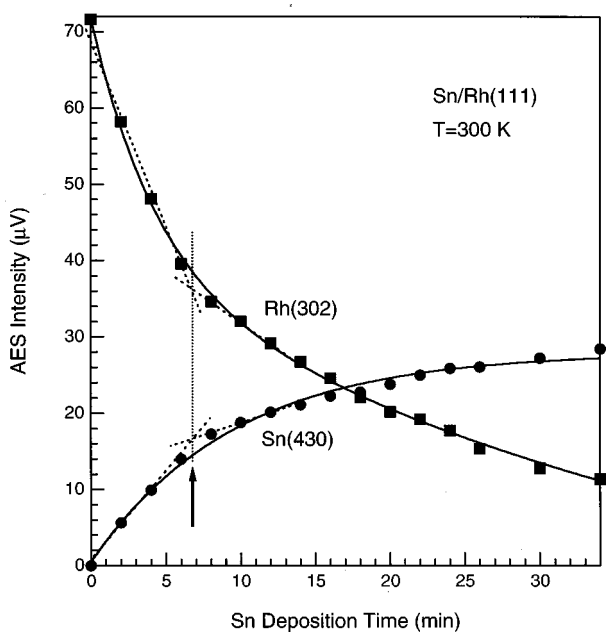

FIG. 2. AES uptake curves obtained from peak-to-peak intensities for Rh (302 eV) and Sn (430 eV) AES signals plotted versus the Sn deposition time. The Rh(111) substrate temperature during Sn deposition was 300 K. The arrow indicates a ''break'' in the uptake curves near 7 min.

about 15-min deposition time, indicating a layer-by-layer growth mode. Fairly sharp changes in the slopes, or ''breaks,'' in both curves occur at about 7-min deposition time. At the break point, the Rh substrate signal has decreased to 52% of its initial value. We can calculate an attenuation of the Rh signal[12] of 52% based on an inelastic mean free path of 5–7 Å for the Rh electrons at 302 eV and a Sn monolayer thickness of 2.5–3.2 Å, respectively, depending on how one estimates the Sn monolayer thickness [using either the interplanar spacing of projected (111)-like planes and Sn-Sn nearest-neighbor distances or a value derived from the average Sn density in bulk Sn]. Thus it may be surmised that the first 7-min exposure corresponds reasonably well to a monolayer of Sn on the Rh surface, with only a small amount of clustering or intermixing. Hereafter, we refer to the 7-min Sn dose as 1 ML of Sn.

At higher exposures of Sn, the AES uptake curves change smoothly, suggesting that Sn is growing in either a Stranski-Krastanov mode [monolayer growth followed by three-dimensional (3D) crystallite growth] or by forming an alloy. Although the deposition time axis in the figure extends only to 35 min, exposures up to 80 min were conducted in which it was found that the Rh signal was never eliminated. Instead, both Sn and Rh signals reached a constant value. The same result was also observed previously elsewhere.[13] These results strongly indicate that alloy formation occurs at room temperature. If pure Sn clustering were occurring on the surface, one would expect the substrate Rh signal to eventually disappear or at least continuously decrease with increasing Sn deposition. We will address this issue in further detail later by examining the Sn growth process via XPD.

In Fig. 3, AES data for two annealing series from different initial coverages of Sn are plotted. The AES data were obtained by using the CMA in the HREELS chamber with

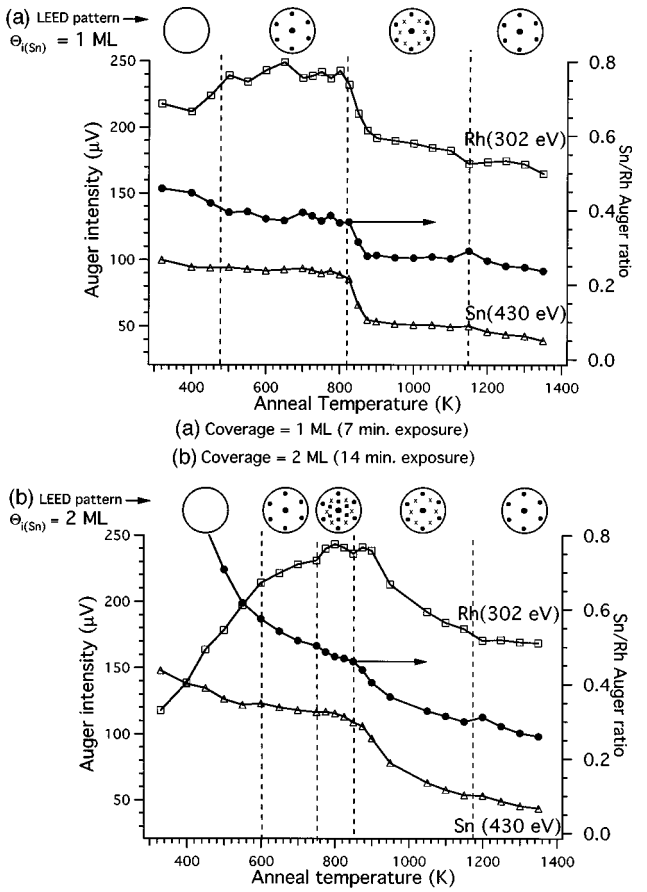

FIG. 3. Annealing studies utilizing LEED and AES of Sn/Rh(111) for two Sn precoverages, as determined from the break in the AES uptake curve: (a) 1 ML of Sn and (b) 2 ML of Sn. The filled circles denote the Sn/Rh AES ratio as indicated on the right-hand axis.

$E_i = 2$ keV and $V_{\mathrm{mod}} = 10V_{pp}$. The two initial coverages were produced by Sn deposition at room temperature, and AES and LEED measurements were made after 2-min annealings at 25–50 K increments in temperature. Prior to this experiment, the Sn doser used on this chamber was calibrated with an AES signal versus exposure curve similar to that in Fig. 2 and the two doses used are those corresponding to the first break points in the curves and twice that deposition time. Since these measurements were made a different chamber, the absolute signal intensities are different from those in Fig. 2.

Considering the top panel in Fig. 3, no LEED pattern was observed at low annealing temperatures (<500 K) because a disordered structure was formed by the vapor-deposited overlayer of Sn. Annealing to 500 K or higher temperatures caused an increase in the Rh AES signal and a (1×1) LEED pattern was observed. The AES intensities and the LEED pattern were stable until annealing temperatures of about 820 K were reached. At these temperatures, a $(\sqrt{3}\times\sqrt{3})R30°$ pattern was formed, and the point at which the $\sqrt{3}\times\sqrt{3}$ spots were first observed coincides with a significant decline in both of the Rh and Sn absolute AES intensities and a decrease in the Sn/Rh AES ratio. We assign this to diffusion of excess Sn away from the surface region and into the bulk of the Rh crystal, leaving behind only the alloy incorporated Sn.

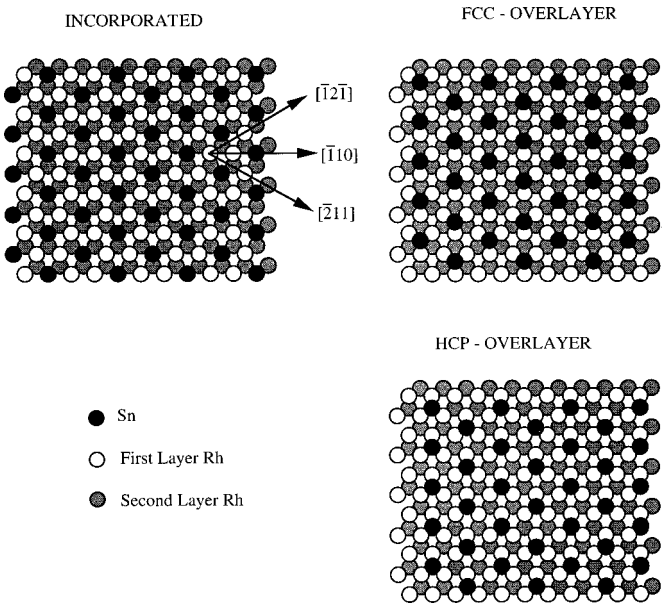

FIG. 4. Models of surface structures proposed for the $(\sqrt{3}\times\sqrt{3})R30°$ LEED pattern. Black circles represent Sn atoms, while Rh atoms indicated by white and gray circles correspond to first- and second-layer atoms, respectively. In an incorporated model, Sn atoms replace the first-layer Rh atoms. In overlayer models, Sn adatoms sit at either fcc or hcp hollow sites.

Finally, the $(\sqrt{3}\times\sqrt{3})R30°$ LEED pattern disappeared at about 1150 K due to either desorption of Sn from the surface alloy or further dissolution into the bulk of the Rh. The Sn/Rh AES ratio was constant over the temperature range of the $(\sqrt{3}\times\sqrt{3})R30°$ LEED pattern, 875–1150 K, indicating that a well-defined surface structure of constant composition can be formed under these conditions. We also note that deposition of a smaller initial coverage of Sn (about 2 min) followed by annealing to 600 K also produced the $(\sqrt{3}\times\sqrt{3})R30°$ LEED pattern.

For a larger initial Sn coverage, as shown in the bottom panel of Fig. 3, large changes occurred in the AES intensities upon heating and a higher temperature of about 600 K was required to form a 1×1 LEED pattern from the surface. The AES changes come about primarily due to clustering of the Sn at these higher temperatures to form larger 3D islands (as will be shown later). The major difference in the two annealing experiments was observed from 750 to 850 K, where a LEED pattern was formed that is consistent with coexisting domains of 2×2 and $(\sqrt{3}\times\sqrt{3})R30°$ structures. Only the $(\sqrt{3}\times\sqrt{3})R30°$ spots were present after 850-K annealing, as at the lower initial Sn coverage, and heating above 900 K caused large decreases in both the Rh and Sn AES signals and a decrease in the Sn/Rh AES ratio. The $(\sqrt{3}\times\sqrt{3})R30°$ LEED pattern did not disappear until about 1175 K, but over the range 900–1175 K the Sn/Rh ratio continued to decrease with increasing temperature. However, the surface formed by heating this Sn film to near 1100 K is probably the same as that in the top panel since the same LEED pattern and Sn/Rh AES ratio is obtained.

All subsequent experiments on the $(\sqrt{3}\times\sqrt{3})R30°$-Sn/Rh(111) surface were performed after preparing the surface using the lower initial deposition (1 ML) of Sn followed by a 2-min annealing at 900 K. This yielded reproducible AES and LEED data for the ordered surface.

TABLE I. C parameter for Na^+-Rh scattering determined from a clean Rh(111) surface. $C_{Na^+\text{-Rh}}=0.80\pm0.03$.

Azimuth	E_0 (eV)	ψ_c (deg)	$C_{Na^+\text{-Rh}}$
[$\bar{1}10$]	400	30.8	0.79
	500	29.9	0.79
	1000	27.5 ± 0.3	0.81–0.83
[$\bar{2}11$]	500	20.7	0.81
	1000	17.5 ± 0.3	0.77–0.79

B. Structure of the $(\sqrt{3}\times\sqrt{3})R30°$-Sn/Rh(111) surface: ALISS studies

1. Proposed structures and scattering potential determination

The three possible structures are shown in Fig. 4. Each of these assumes that the $(\sqrt{3}\times\sqrt{3})R30°$ unit cell arises from a basis of one Sn atom per unit cell. The incorporated, i.e., alloy, model corresponds to replacing $\frac{1}{3}$ of the first layer Rh atoms with Sn atoms. In the overlayer models, the Sn atoms are placed as adatoms occupying either the fcc sites or the hcp sites. These models will guide our discussion of the ALISS data and inevitably one of them (the alloy) will account for the $(\sqrt{3}\times\sqrt{3})R30°$ structure.

As demonstrated in previous ALISS studies,[6,7] it is essential to first determine the scattering potential (Thomas-Fermi-Moliare potential) between the incoming ion and the surface atoms. A detailed discussion of this problem can be found in Ref. 14. In our case, there are two parameters that have to be determined: $C_{Na^+\text{-Rh}}$ and $C_{Na^+\text{-Sn}}$. It is worthwhile to point out that the ALISS technique can be calibrated internally; these C parameters can be derived from the experiment itself. The C parameter for Na^+ and Rh scattering can be determined easily from the clean Rh(111) surface. Table I gives the $C_{Na^+\text{-Rh}}$ values derived from different azimuths and different ion-beam energies. These values are very consistent and converge to an average value of $C_{Na^+\text{-Rh}}=0.80\pm0.03$. Since all three models possess the same Sn atom chains along the [211] direction, the other C parameter is determined in a similar fashion based on this azimuth from the $(\sqrt{3}\times\sqrt{3})R30°$ surface. The derived values of $C_{Na^+\text{-Sn}}$ for different ion-beam energies are tabulated in Table II, yielding $C_{Na^+\text{-Sn}}=0.76\pm0.04$.

2. Surface structure: Alloy versus overlayer Sn

Figure 5 shows the energy spectra for 1-keV Na^+ incident on the $(\sqrt{3}\times\sqrt{3})R30°$-Sn/Rh(111) surface, as well as on

TABLE II. C parameter for Na^+-Sn scattering determined from a $(\sqrt{3}\times\sqrt{3})R30°$-Sn/Rh(111) surface. $C_{Na^+\text{-Sn}}=0.76\pm0.04$.

Azimuth	E_0 (eV)	ψ_c (deg)	$C_{Na^+\text{-Rh}}$
[$\bar{2}11$]	500	19.2	0.79
	1000	16.7 ± 0.3	0.73–0.77
	2000	14.7	0.72

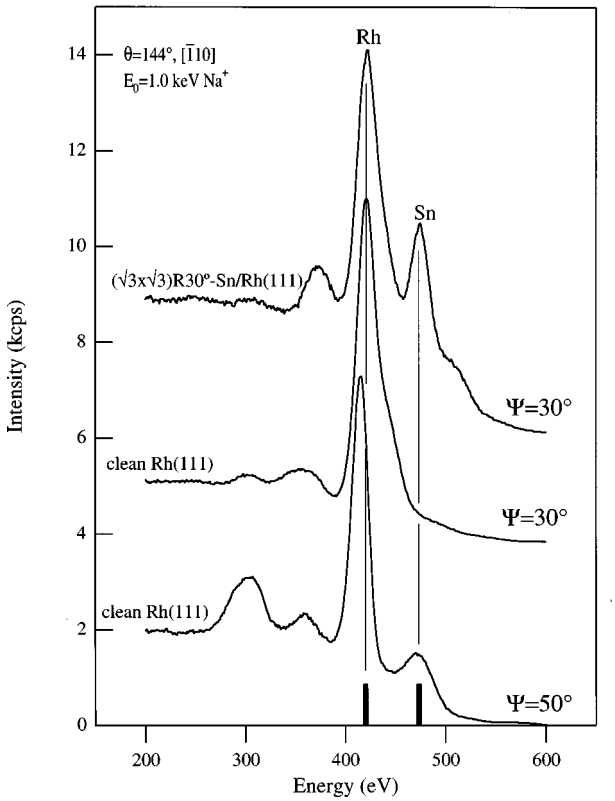

FIG. 5. Energy spectra of 1-keV Na^+ scattered from the clean Rh(111) and $(\sqrt{3}\times\sqrt{3})R30°$-Sn/Rh(111) surfaces in the [110] direction. The total scattering angle is 144°. Strong interference to the Sn scattering from the Rh background can be seen clearly from the clean Rh(111) curves at two different polar angles. The $\sqrt{3}$ alloy for this and subsequent ALISS experiments was prepared by deposition of 1 ML of Sn followed by a 2-min annealing at 900 K.

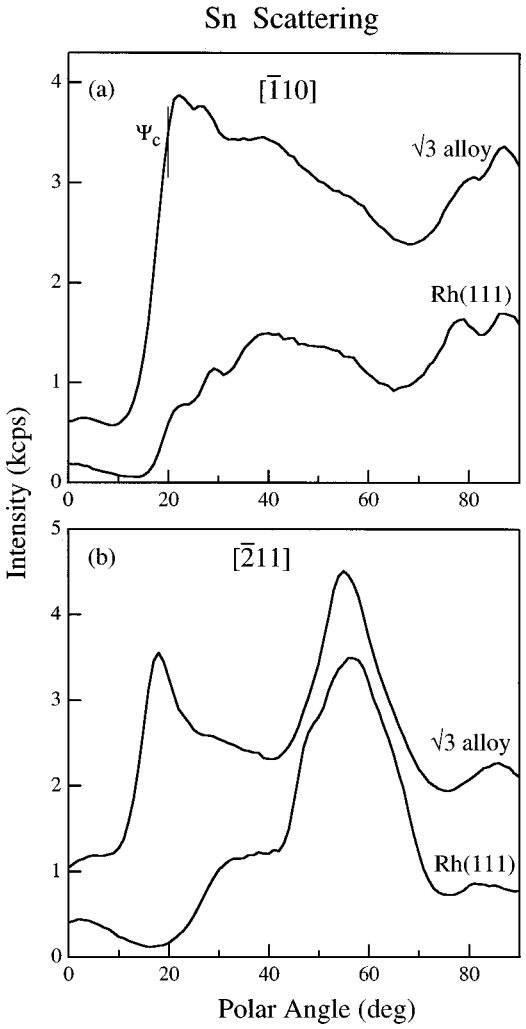

FIG. 6. Polar-angle scans of 1-keV Na^+-Sn scattering on the $(\sqrt{3}\times\sqrt{3})R30°$ surface are shown along two different azimuths. Along with each scan is the Sn ''blank'' scan taken on the clean Rh(111) substrate (a) along the short ([110]) azimuth and (b) along the long ([211]) azimuth.

clean Rh(111) surfaces. The observed scattering peak features from the Rh atoms extend into the region of the Sn peak, particularly at higher polar angles. This indicates that the actual contributions from the Sn scattering overlap with this Rh background. To test how this affects the single scattering from Sn, ''blank'' Sn scans from a clean Rh(111) substrate were conducted. These scans indicate that the Rh backgrounds are fairly flat at polar angles below 20°, but larger peak modulations occur at the higher polar angles. This suggests that great care must be taken in the interpretation of the Sn-scan peaks at the larger polar angles. Also seen in Fig. 5 is the shift in the Rh binary scattering peak by as much as 6 eV, particularly for polar angles above 30°. The ion energy analyzer has an energy window size of ± 12 eV, which helps to minimize this shift problem. In addition, we tried to check this influence by offsetting the analyzer energy on purpose over several electron volts, and no significant effect was observed on the angular scans.

The polar angle scans from Sn single scattering as well as blank scans taken at 1-keV Na^+ are shown in Fig. 6. Along the short ([110]) azimuth, a critical angle of Na^+-Sn scattering of $\psi_c = 20°$ was obtained. This critical angle is very different from what is expected from any of the overlayer models. Given the much larger Sn-Sn atom spacing in both fcc and hcp overlayer models, a much smaller critical angle ($\psi_c \sim 10°$) is expected based on calculations. This leaves no choice but to opt for the alloy model. It will be shown that the alloy model can consistently explain all of the scattering features from both Rh and Sn scattering along all of the different azimuths studied.

In the alloy model, the topmost layer is composed of $\frac{1}{3}$ of Sn rows and $\frac{2}{3}$ of Rh rows along the long azimuths ([211] or [121]). The Sn rows produce the scattering feature observed in Fig. 6(b). As pointed out before, features at larger polar angles do not necessarily correspond to real Sn scattering; their existence could be the result of interference from Rh scattering.

The polar angle scans from Rh are shown in Fig. 7. As expected, the scattering features from the long azimuths ([211] or [121]) are almost unaltered between the clean Rh surface and $(\sqrt{3}\times\sqrt{3})R30°$ alloy surface. The peak intensities at 18° are reduced to 62–64 % compared to the clean Rh(111) substrate. This is in good agreement with the assessment[13] that the number of first-layer Rh atoms in the alloy is $\frac{2}{3}$ of that on the clean Rh(111) substrate. Along the short azimuth ([110]), the polar scans for clean Rh(111) and the $(\sqrt{3}\times\sqrt{3})R30°$ alloy are noticeably different. The peak at

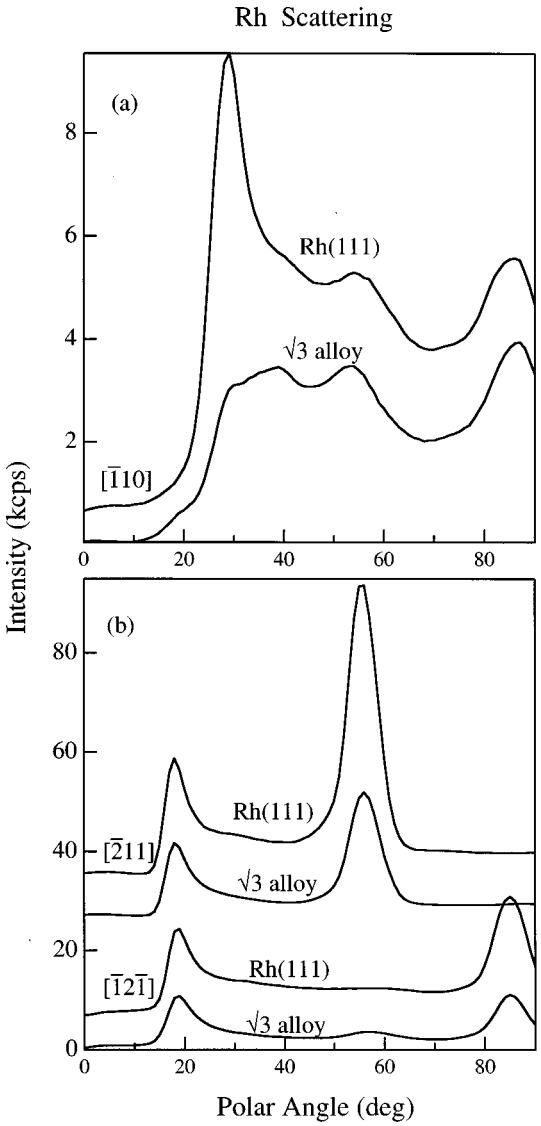

FIG. 7. Polar-angle scans of 1-keV Na^+-Rh scattering on the $(\sqrt{3}\times\sqrt{3})R30°$ surface are shown along two different azimuths. Accompanying each scan is one taken on a clean Rh(111) substrate (a) along the short azimuth ([110]) and (b) along the long azimuths ([211] or [121]).

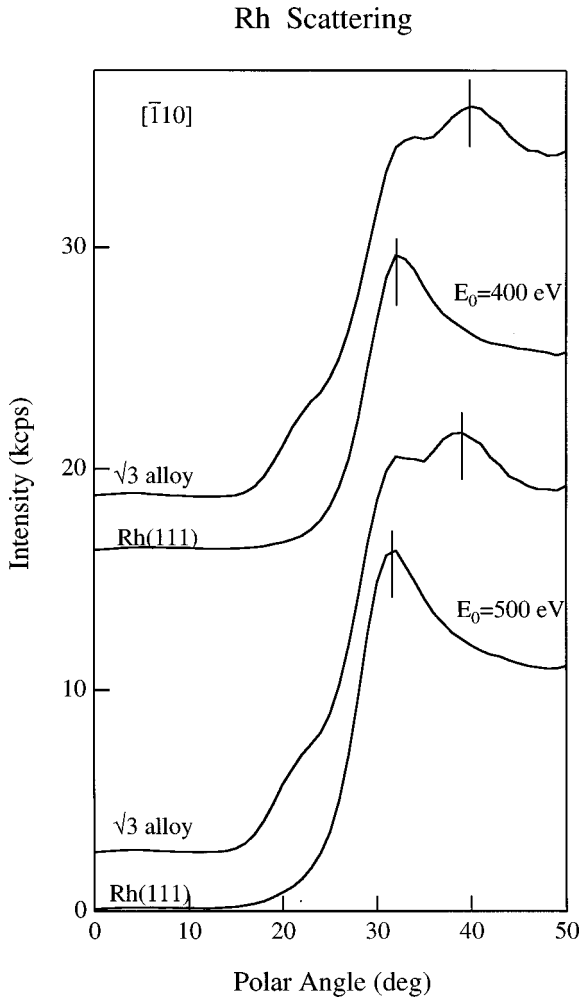

FIG. 8. Polar-angle scans of Na^+-Rh scattering on the $(\sqrt{3}\times\sqrt{3})R30°$ surface are shown at incident Na^+ beam energies of $E_0 = 400$ and 500 eV. Along with each scan is one taken on the clean Rh(111) substrate. Each pair of peaks marked by the bars at a particular incident energy are differentiated by either Rh-Rh or Sn-Rh being the shadowing-target atom pair.

29° is greatly reduced and a new feature evolves around 35°. The intensity reduction of the 29° peak can be explained by the effect of buckling, where the Sn atoms are displaced upward compared to the Rh atoms instead of being coplanar on the alloy surface. A similar angular spectrum was observed on the Sn/Ni(100) system as well.[6] One-third of the Rh atoms will be shadowed directly by the buckled neighboring Sn atoms, which will shift the 29° peak to higher polar angles. The remaining $\frac{1}{3}$ of the Rh atoms will still be shadowed by neighboring Rh atoms and thus the original peak should still be seen at 29°, but with only $\frac{1}{3}$ of its original intensity. As a matter of fact, the observed peak intensity at 29° for the alloy is reduced to 33% of the value on Rh(111), which correlates well with the predicted result. The new peak formed in the polar scan due to the buckled Sn atoms can be seen better in Fig. 8, where polar angle scans at two different primary ion-beam energies are compared. We can tell clearly that the new peak is formed at 7°–8° higher polar angle. This offset corresponds directly to the buckling angle and thus it can be used to estimate the buckling distance. We obtain a value for the Sn outward buckling distance of 0.32 Å by assuming that the Sn atoms sit at Rh(111) positions laterally, but due to buckling are displaced above the Rh surface plane so that a line between the Sn and Rh centers makes an angle of 7.5° with the Rh plane.

A better estimate of the Sn buckling distance can be obtained from the Sn scattering along the short azimuth [110] as shown in Fig. 6(a). The critical angle ψ_c is closely related to the vertical distance between Sn and a nearest-neighbor Rh atom. If the dependence of the critical angle ψ_c on the buckling distance d_p were known, we could determine the value of d_p from the experimentally measured value of ψ_c. A plot of the critical angle ψ_c versus the buckling distance d_p is given in Fig. 9. This plot was obtained by performing a chain simulation using the MARLOWE code[14] to include the interactions of all nearby atoms in the full crystal. Measurements at four different ion beam energies were carried out, each providing its own critical angle. The results consistently indicate a value of $d_p = 0.29 \pm 0.05$ Å. Our prior independent

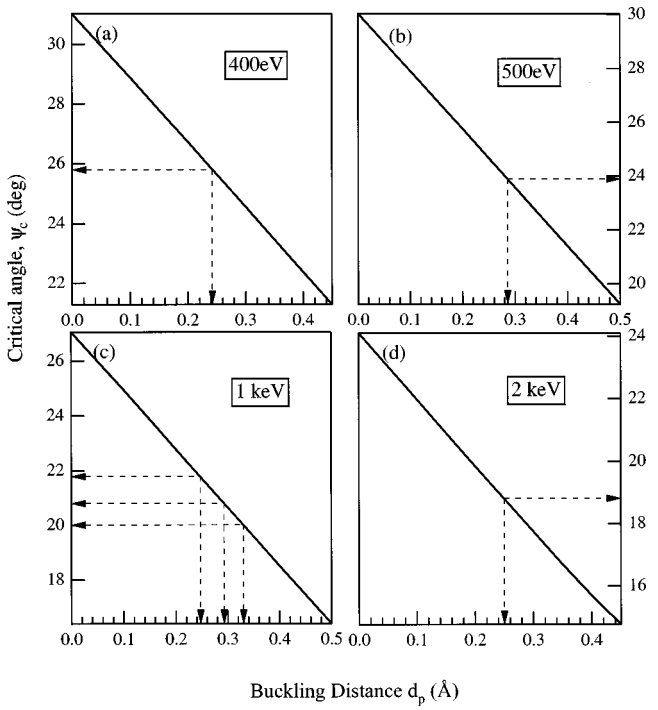

FIG. 9. Calculated critical angles expected for the perpendicular height of the Sn atom buckling distance in the $(\sqrt{3}\times\sqrt{3})R30°$ surface are shown as solid curves. The measured critical angles and the derived buckling distances are indicated by the dashed lines using (a) $E_0=400$ eV Na^+, (b) $E_0=500$ eV Na^+, (c) $E_0=1.0$ KeV Na^+, and (d) $E_0=2.0$ keV Na^+.

estimate of $d_p=0.32$ Å falls within the error bars of this determination.

We have no clear explanation for the Rh scattering feature that appears around a polar angle of 19° in the scans from the $\sqrt{3}$ alloy in Figs. 7 and 8. This peak could be attributed to rippling of the Rh atoms, but other possible explanations such as Sn sites that are not occupied, i.e., a Rh surface vacancy, or rippling induced by subsurface Sn can be ruled out.

3. Surface stoichiometry: Sn coverage for the $(\sqrt{3}\times\sqrt{3})R30°$ alloy

A tacit assumption for the proposed structures in Fig. 4 is that there are $\frac{1}{3}$ ML of Sn atoms and $\frac{2}{3}$ ML of Rh atoms on the surface. An identical LEED pattern can be formed as well by putting $\frac{2}{3}$ ML of Sn atoms and $\frac{1}{3}$ ML of Rh atoms on the surface. These two different situations relate directly to the Sn coverage on the outermost layer. Possible structures for this case are essentially the same as those shown in Fig. 4, but with the Sn and Rh atom labels transposed at the surface. This is an extremely important aspect of the surface structure and this issue should be addressed as directly as possible.

There is clear evidence against the choice of a Sn-rich $(\sqrt{3}\times\sqrt{3})R30°$ surface alloy. If this were the case, the Sn polar scan along the short azimuth [110] would be characterized by two low-angle peaks in Fig. 6(a). One of them would be caused by the Rh-Sn atom pair as before, while the other one would be induced by the Sn-Sn atom pair. The latter peak would appear at a much higher polar angle at about 29°. Furthermore, in the Rh polar angle scan along the short azimuth in Fig. 7(a), the 29° peak would not exist for the alloy since the Rh atoms would be solely shadowed by Sn atoms. These effects were never observed in our experiments and thus we can eliminate the Sn-rich surface models from consideration.

C. Characterization of the Sn/Rh(111) surface alloy by XPS

We utilized XPS to probe changes in the electronic structure of the surface due to alloying. The results of these grazing incidence (20°) XPS studies on the $(\sqrt{3}\times\sqrt{3})R30°$-Sn/Rh(111) surface alloy, along with comparison measurements for Rh(111) and a thick condensed film of Sn, are summarized in Table III(a). The Sn film values were obtained from deposition on Pt(111), as discussed below. Binding energies referenced to the Fermi level are reported for several core levels and also for the valence band. The x-ray excited Auger transitions were also measured and the principal Auger peaks were used to calculate Auger parameters. Peak positions were determined by fitting simulated curves using contributions of Gaussian and Lorenztian line shapes through the raw data. Since the SCA was equipped with a multichannel detector, the spectra were obtained with a good signal-to-noise ratio and good fits of the data were obtained. The spectrometer work function was adjusted to define Rh $3d_{5/2}=307.20$ eV binding energy (BE) for clean Rh(111). Emission from the Rh valence band (VB) can be characterized by the centroid BE, and this shows a shift of -0.30 eV upon alloying. The VB maximum, however, shows a 0.30-eV shift upon alloying, indicating a narrowing in the valence-band emission. All of the Rh core levels measured show either very small or negative-binding-energy shifts. The Rh $3d_{5/2}$ level shifts -0.35 eV upon alloying, with only a -0.10-eV change in the $3d$ spin-orbit splitting. The Rh $3d_{3/2}$ peak suffers from overlap with the Sn $3d_{3/2}$ peak, but values for the Rh $3p$ peaks are fairly consistent with the behavior of the Rh $3d$ peaks. The Rh Auger parameter, obtained as the difference between the binding energy of the Rh $3d_{5/2}$ peak and the apparent binding energy of the highest kinetic-energy Rh Auger transition, shows a larger shift of -0.65 eV upon alloying. A shift of the Auger parameter to more negative values is usually interpreted as indicating a lower oxidation state (larger negative charge) on the probed atom. The Sn $3d$ core levels show a larger negative shift of -0.60 eV upon alloying, referenced to a thick Sn film standard, with no change in the $3d_{3/2}$-$3d_{5/2}$ splitting. The highest-kinetic-energy Sn Auger transition shifts to 0.23 eV lower apparent binding energy and the Sn Auger parameter shifts -0.37 eV upon alloying.

We also provide in Table III(b) XPS results for Pt(111), a thick Sn film, and the $(\sqrt{3}\times\sqrt{3})R30°$-Sn/Pt(111) surface alloy for comparison with the above Rh-Sn results. The Sn film was formed by vapor deposition onto the Pt substrate at 200 K until the Pt $4f$ peaks were reduced to less than 1% of their value on clean Pt(111). Calibration of the spectrometer work function was obtained by defining Pt $4f_{7/2}=71.20$ eV BE for clean Pt(111). The Pt VB is characterized by two maxima, at 1.65- and 3.91-eV BE, with a centroid at 3.1-eV BE. Alloying caused these maxima to shift to higher BE and the VB emission to narrow by about 0.6 eV. Smaller core-

TABLE III. XPS results for (a) Rh(111) and the $(\sqrt{3}\times\sqrt{3})R30°$–Sn-Rh alloy [the Auger parameters $\alpha' = E_b(\text{Rh } 3d_{5/2}) - E_b(\text{Rh } M_{45}VV)$, and $\alpha'' = E_b(\text{Sn } 3d_{5/2}) - E_b(\text{Sn } M_4N_{45}N_{45})$ and the values in parentheses denote signals that are less certain because of overlapping peaks or poorer signal-to-noise ratios] and (b) Pt(111) and the $(\sqrt{3}\times\sqrt{3})R30°$–Sn-Pt alloy [the Auger parameters $\alpha' = E_b(\text{Pt } 4f_{7/2}) - E_b(\text{Pt } N_4N_{67}N_7)$, and $\alpha'' = E_b(\text{Sn } 3d_{5/2}) - E_b(\text{Sn } M_4N_{45}N_{45})$] (the BE E_b is in eV and $\mathcal{V}$ denotes the VB).

Core level	Rh(111)	(a) Sn	$(\sqrt{3}\times\sqrt{3})R30°$ alloy	BE shift
Rh($\mathcal{V}$)	2.50		2.20	−0.30
Rh($4p$)	47.40		47.48	0.08
Rh($3d_{5/2}$)	307.20		306.85	−0.35
Rh($3d_{3/2}$)	312.25		311.80	−0.45
$\Delta(3d_{3/2}$-$3d_{5/2})$	5.05		4.95	−0.10
Rh($3p_{3/2}$)	496.50		(496.1)	(−0.4)
Rh($3p_{1/2}$)	520.90		520.97	0.07
$\Delta(3p_{3/2}$-$3p_{1/2})$	24.40		(24.9)	(0.5)
Rh($3s$)	(628.5)		(628.3)	(−0.2)
Rh($M_{45}VV$)	951.40		951.70	0.30
$\alpha' + h\nu$	609.40		608.75	−0.65
Sn($3d_{5/2}$)		485.25	484.65	−0.60
Sn($3d_{3/2}$)		493.90	493.30	−0.60
$\Delta(3d_{3/2}$-$3d_{5/2})$		8.65	8.65	0.00
Sn($M_4N_{45}N_{45}$)		816.28	816.05	−0.23
$\alpha'' + h\nu$		922.57	922.20	−0.37

Core level	Pt(111)	(b) Sn	$(\sqrt{3}\times\sqrt{3})R30°$ alloy	BE shift
Pt($\mathcal{V}$)	1.65, 3.91		1.96, 4.14	0.31
Pt($5p_{3/2}$)	52.23		52.41	0.18
Pt($4f_{7/2}$)	71.20		71.20	0.00
Pt($4f_{5/2}$)	74.60		74.70	0.10
$\Delta(4f_{5/2}$-$4f_{7/2})$	3.40		3.50	0.10
Pt($4d_{5/2}$)	314.50		314.50	0.00
Pt($4d_{3/2}$)	331.60		331.70	0.10
$\Delta(3d_{3/2}$-$3d_{5/2})$	17.10		17.20	0.10
Pt($4p_{3/2}$)	519.45		519.90	0.45
Pt($N_4N_{67}N_7$)	1084.40		1084.43	0.03
$\alpha' + h\nu$	240.40		240.37	−0.03
Sn($3d_{5/2}$)		485.25	485.28	0.03
Sn($3d_{3/2}$)		493.90	493.98	0.08
$\Delta(3d_{3/2}$-$3d_{5/2})$		8.65	8.70	0.05
Sn($M_4N_{45}N_{45}$)		816.28	816.53	0.25
$\alpha'' + h\nu$		922.57	922.35	−0.22

level shifts were observed for the Pt levels upon alloying compared to the Rh-Sn results. Either no shift or very small (0.10 eV) positive shifts occur for the Pt $4f$ and Pt $4d$ levels upon alloying. The Pt $4p_{3/2}$ apparently shows a larger positive shift. Consistently, the Pt Auger parameter shows essentially no change upon alloying. These data should be compared to a recent study of the surface core-level shift (SCLS) for this same alloy, in which the Pt $4f_{7/2}$ SCLS is equal to −0.37 and −0.25 eV on the Pt(111) and $\sqrt{3}$-Sn/Pt(111) surface alloy, respectively, indicating a shift of the surface Pt $4f_{7/2}$ level of 0.12 eV upon alloying with Sn.[15] The Sn core levels also show much smaller changes than were seen for the Rh-Sn alloy and only a small shift to higher binding energy was observed. A small shift occurs for the Sn $M_4N_{45}N_{45}$ Auger transition upon alloying so that the change in the Sn Auger parameter is smaller than that for Rh-Sn, but the change has the same sign for both the Rh and Pt alloys.

These changes described above in the XPS spectra reveal that the Rh-Sn bonding interaction is larger than that for Pt-Sn, with the small shifts probably arising from the rehybridization that occurs during bonding in the intermetallic compounds. We propose that little charge transfer occurs in either case, although Sn (1.72) is more electronegative than Pt (1.44) or Rh (1.45) according to the Allred-Rochow formula.

D. Depth of alloyed Sn atoms: An XPD study

The discussion of the depth of Sn atoms involved in the $(\sqrt{3}\times\sqrt{3})R30°$ alloy will address two issues. The first is the

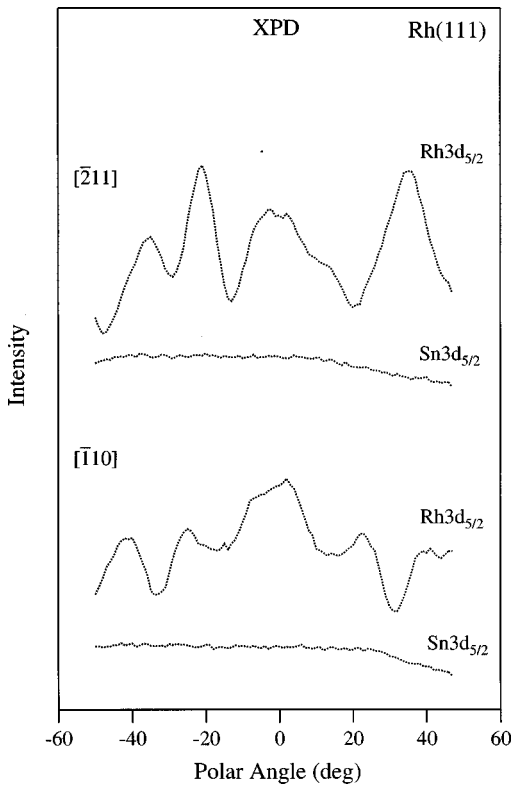

FIG. 10. The angular dependence of Rh $3d_{5/2}$ emission on a clean Rh(111) substrate is shown along [211] and [110] azimuths. Along with each of these scans is the blank scan conducted at the photoelectron energy of the Sn $3d_{5/2}$ emission. The polar angles ψ defined here are referenced to the surface normal, i.e., $\psi=0°$ lines up the detector with the surface normal.

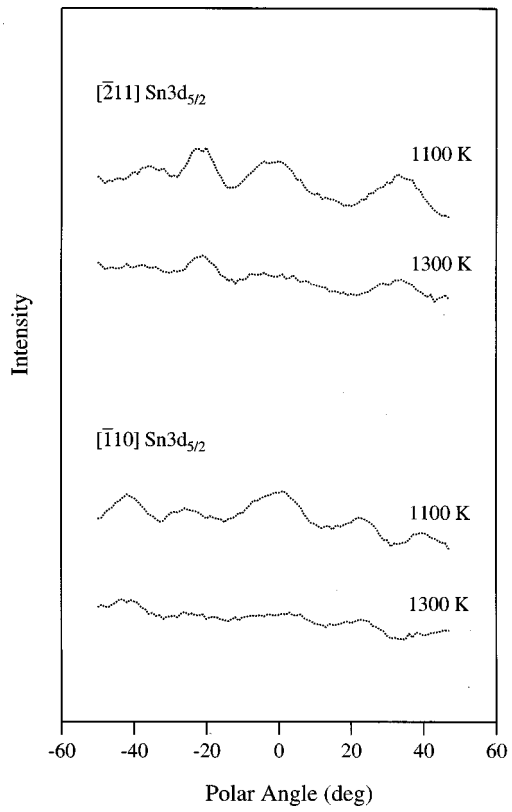

FIG. 11. The angular dependence of the Sn $3d_{5/2}$ emission is shown along the [211] and [110] azimuths after annealing the $(\sqrt{3}\times\sqrt{3})R30°$ surface to different temperatures. The initial Sn coverage was 4 ML deposited at room temperature.

possibility of constructing a strictly 2D surface alloy and the second is the determination of the registry of the Sn atoms underneath the first layer if they do exist. Under favorable conditions, these questions can be answered by ALISS itself. The higher angle peaks in the polar angle scans normally relate directly to the subsurface scattering process. Although such Sn scattering peaks were observed in Fig. 6, we cannot rule out the possible scenario of Rh scattering interference. If these peaks were indeed the results of Sn scattering, the subsurface Sn atoms would have the same registry as the substrate Rh atoms. This can be concluded from the similar polar angle for the higher angle peak observed in the corresponding Rh polar scans.

A much better tool to apply in this case is XPD. Figure 10 shows the polar-angle dependence of the Rh $3d_{5/2}$ and the Sn $3d_{5/2}$ (blank scan) photoelectron emission intensities from the clean Rh(111) substrate. To comply with the usual convention in XPD, we have changed the notation of the polar angle in our XPD data to refer to the angle off of the surface normal as opposed to off of the surface plane as in ALISS. The blank scan in Fig. 10 is essentially flat, and thus the Rh background is not expected to interfere with the Sn scan features. The Sn $3d_{5/2}$ polar-angle dependence taken after annealings to different temperatures are shown in Fig. 11. The surface for these studies was prepared at room temperature with an initial deposition of 4 ML of Sn. After annealing to both temperatures, the $(\sqrt{3}\times\sqrt{3})R30°$ LEED patterns are very sharp. Two conclusions can be drawn from these results. First, it is a simple matter to determine that subsurface Sn atoms occupy the Rh sites by comparing the Sn $3d$ angular distributions with those accompanying Rh $3d$ emission. Virtually identical diffraction modulation is observed in the Sn $3d$ and Rh $3d$ angular scans. Second, the large reduction in the intensity of the angular modulation once the sample has been annealed to 1300 K indicates that the amount of subsurface Sn in the near-surface region is much less than that at 1100 K. The $(\sqrt{3}\times\sqrt{3})R30°$ surface alloy prepared in the manner described above exists with significant amounts of subsurface Sn in the second layer if the annealing temperature is not high enough, such as in the 1100-K annealing case here. By annealing to even higher temperatures, the modulation features seen here almost disappear. This indicates that it is possible to form a strictly 2D $(\sqrt{3}\times\sqrt{3})R30°$ surface alloy by extensive high-temperature annealing.

We have discussed thoroughly the structural issues regarding the $(\sqrt{3}\times\sqrt{3})R30°$-Sn/Rh(111) surface. This surface, derived from high-temperature annealing, exists as an alloy phase that is characterized by the outward buckling of Sn atoms above the Rh atom surface layer. We also conjecture that alloy formation can occur at temperatures as low as room temperature based on the AES data. The following section will address some Sn deposition and film growth issues on the Rh(111) substrate at room temperature.

E. Growth of Sn on Rh(111) at 300 K: Clustering or alloying?

The AES uptake curves, in which a finite and constant Rh signal was observed once more than 10 ML of Sn was de-

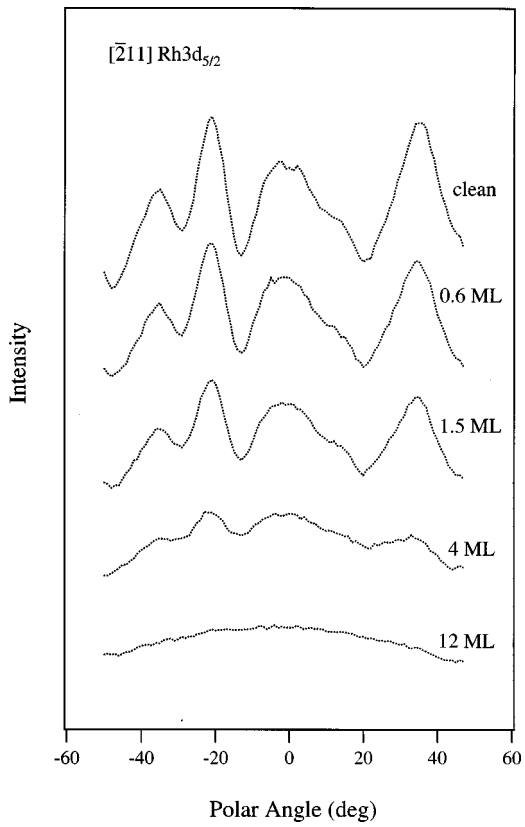

FIG. 12. The angular dependence of the Rh $3d_{5/2}$ emission is shown in the [211] for direction at different initial Sn coverages. Sn deposition was carried out at room temperature in each case and the curves were measured at the same temperature.

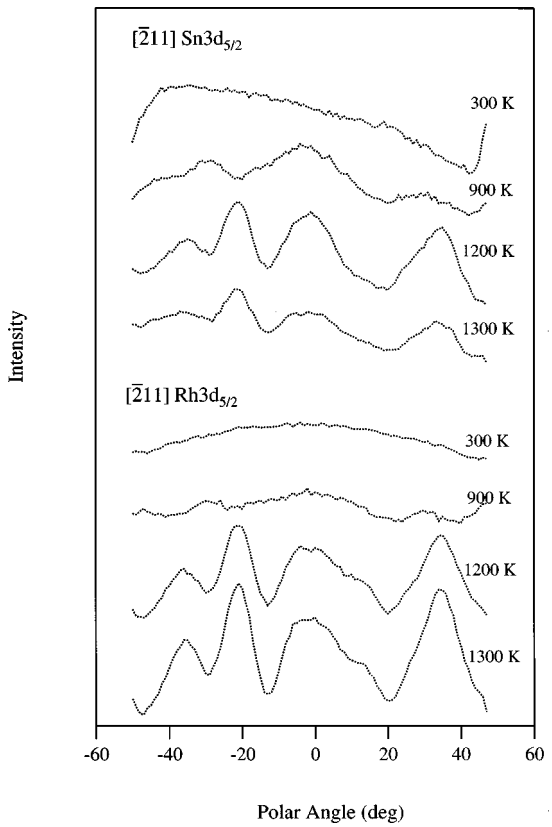

FIG. 13. The angular dependence of Sn $3d_{5/2}$ and Rh $3d_{5/2}$ emission is shown after annealing the surface to elevated temperatures. Deposition at room temperature provided an initial Sn coverage of 12 ML. Annealing to 1300 K produces the $(\sqrt{3}\times\sqrt{3})R30°$ LEED pattern.

posited, cannot be explained solely by a pure Sn cluster growth mechanism. The failure to totally eliminate the Rh signal cannot be explained by cluster growth alone. This is due to the fact that the clusters are expected to grow three dimensionally and eventually eliminate the substrate Rh signal. A much better experiment involves the use of XPD to distinguish between clustering and alloy growth. In the pure clustering model, the detected Rh signal will come directly from the bulk Rh contribution and its emission possesses the clean Rh signature. However, in the alloy case, this substrate signature should disappear in the Rh emission. Thus, by comparing the Rh angular dependence from a thick Sn film with that from the clean substrate, we should be able to distinguish both cases.

Figure 12 shows the results of such an experiment. Different thicknesses of Sn films were prepared at room temperature and the XPD experiments were conducted after deposition. No LEED patterns were found during Sn film growth. The most obvious result evident in Fig. 12 is the loss of the diffraction modulations of substrate Rh atoms once about 4 ML of Sn was deposited. This indicates that pure cluster growth of Sn is not the growth process. For substrate Rh atoms buried deeper than about 4–5 atomic layers below the surface, the forward-scattering enhancements are largely eliminated by multiple scattering. Thus the observed Rh emission must be from the Rh atoms that are intermixed with Sn atoms. Further support for this physical model is the presence of a constant Rh Auger signal intensity and the presence of Rh scattering intensity in the ISS spectra, even after much thicker (>10 ML) Sn films were deposited at room temperature. These data also rule out an Stranski-Krastanov (monolayer plus cluster) growth mechanism. Another important characteristic of these polar dependences is the roughly isotropic behavior of both Rh and Sn emissions once the 4–5 ML of Sn were deposited. This shows that the growth at room temperature does not proceed epitaxially, but rather as a random, disordered alloy. This random alloy possesses a constant stoichiometry for the Sn and Rh components, although Sn atoms comprise the predominant part. This latter conclusion was derived from the constant Sn and Rh AES intensities once the deposited Sn amount exceeds a certain thickness.

The above observations indicate that Rh-Sn intermixing occurs during the deposition of thick (>1 ML) Sn films on Rh(111) at 300 K. It is also interesting to explore the stability of this alloy arrangement with increasing temperatures. Figure 13 shows the polar-angle scans after annealing an initial Sn deposition of 12 ML. Below 1200 K, no LEED pattern was observed. After annealing to 1200 K for 30 sec, a combination of $(\sqrt{3}\times\sqrt{3})R30°$ and 2×2 LEED patterns appeared. Subsequent annealing to 1300 K produced a sharp $(\sqrt{3}\times\sqrt{3})R30°$ pattern. Upon annealing to 900 K, we still observed the flat angular features from Rh emission, but an intensity modulation for Sn emission appeared. Moreover, the Rh intensity was increased by 50% and the Sn intensity was reduced by nearly 25%. These observations indicate that the thickness of the original alloy film is greatly reduced

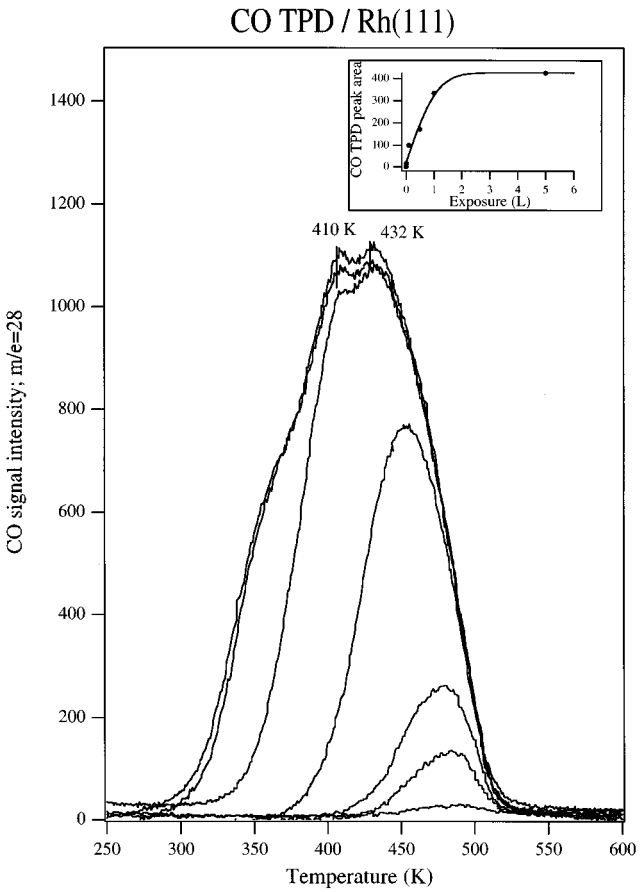

FIG. 14. CO TPD from Rh(111). The heating rate used was 10 K/s.

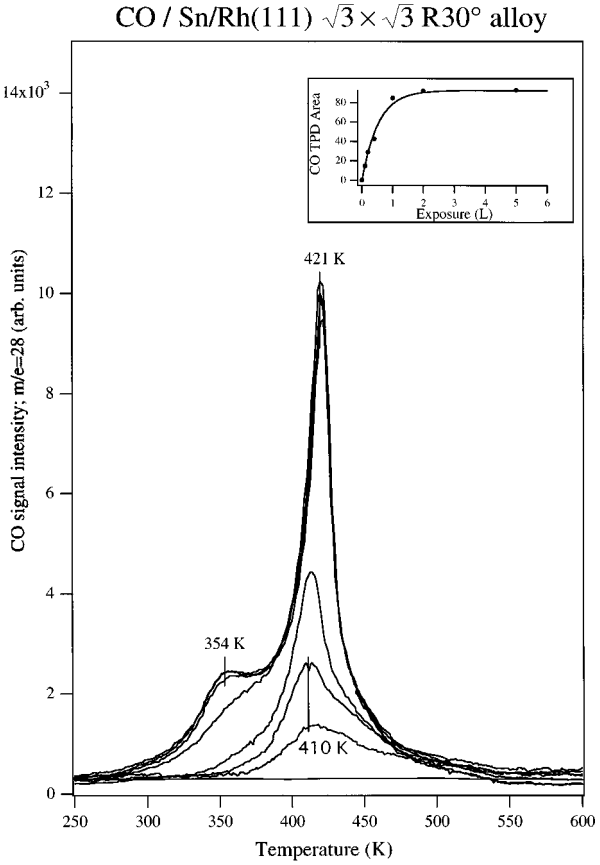

FIG. 15. CO TPD from the $(\sqrt{3}\times\sqrt{3})R30°$-Sn/Rh(111) alloy surface. The heating rate used was 14 K/s.

upon annealing. It is likely that interdiffusion occurred and an intermetallic compound was formed. The $(\sqrt{3}\times\sqrt{3})R30°$ surface alloy that can be formed at 1300 K is accompanied by subsurface Sn atoms as indicated by the strong modulations.

F. Probing the surface chemistry of Rh-Sn surface alloys: CO chemisorption

TPD spectra for increasing CO exposures on the Rh(111) surface at 100 K are shown in Fig. 14. An inset shows the CO uptake curve constructed from this data. On Rh(111), CO desorption first occurs at a peak at 483 K at low coverage and then this peak decreases to 432 K with increasing coverage. Using Redhead analysis,[16] one can estimate that these temperatures correspond to desorption activation energies (E_d) ranging from 29 to 26 kcal/mol, which agrees well with previous results.[17,18] At higher coverages a peak at 410 K is formed along with some broadening in the peak to lower temperatures at near saturation coverages. This more weakly bound state has $E_0 \sim 24.5$ kcal/mol. HREELS experiments[19] have assigned the high-temperature peak to bonding of CO at atop sites and the 410-K peak to bonding of CO at bridge sites.

CO TPD spectra from the $\sqrt{3}$-Sn/Rh(111) surface alloy are shown in Fig. 15. Desorption of CO at low coverage occurs in a peak at 410 K, with a high-temperature tail probably due to defect sites of unalloyed Rh. The CO desorption peak shifts up in temperature to 421 K with increasing coverage. Near saturation coverage, a small additional desorption peak at 354 K develops. Since the peak at 421 K is so narrow, desorption from the alloy is mainly restricted to one type of binding site. This is most likely the atop site since that is the strongest bonding site on clean Rh(111) and the formation of the alloy reduces more the number of bridge sites (50%) compared to the number of atop sites (33%). The relatively small shift in desorption peak temperature and the value of E_d (24.5–25 kcal/mol) suggests that the main effect of alloyed Sn on CO chemisorption on this Rh-Sn surface alloy is to block sites. This small shift in the CO adsorption energy is also consistent with the small changes observed in the XPS studies reported above, ruling out large changes in the Rh electronic structure in the alloy. The addition of alloyed Sn to the Rh(111) surface reduces the total coverage of CO by about a factor of 4. Additional studies by LEED and HREELS are needed to further determine the effect of alloyed Sn on the binding site of CO on the alloy surface.

IV. DISCUSSION

Although we can rule out a pure Sn 3D crystallite growth mode, we cannot exclude growth involving both clustering and alloying. In fact, the combination of both processes might better explain the AES uptake seen in Fig. 2. Alloying at room temperature has rarely been noted, but recently more and more systems have been seen to behave in such a manner. The Sn/Ni(100) system[6] that we previously studied was

found to form an alloy at 250 K and the strong interdiffusion even arranges the alloy surface in a $c(2\times2)$ structure. For the Fe/Ag(100) system,[20] the Fe atoms undergo place exchange with Ag atoms in the top layer of Ag(100) at an even lower temperature of 100 K. For the case studied in the present work, that of the Sn/Rh(111) system, the intermixing is very sensitive to the temperature. At room temperature, a multilayer alloy is formed with a dominant Sn component. At high temperature, the intermixing is more extensive and eventually leads to a 2D surface alloy characterized by $\frac{1}{3}$-ML-Sn concentration.

Our assignment of 1 ML of Sn at the 7-min break point in the AES uptake is based on the attenuation of the Rh substrate signal that is consistent with a simple calculation for the decrease in intensity expected for a 1-ML-thick Sn overlayer film. Of course this is not a rigorous determination and it could be incorrect, considering that alloy formation clearly occurs at higher Sn coverages at room temperature. (However, we note that the Sn monolayer may be more stable against alloying than thicker Sn films due to an increased solubility of Rh in Sn for thicker layers.) It is clear that it is difficult to determine the Sn coverage to which the break in Fig. 2 corresponds. It is possible that the break is related to the finishing of the first Sn-Rh alloy layer. AES and Rutherford-backscattering spectroscopy measurements made by Paffett[13] suggest a Sn density of 1.0×10^{15} atoms/cm^2 at the break, which is about $\frac{2}{3}$ ML of Sn atoms if a closest-packed arrangement is assumed. Furthermore, the Sn AES intensity obtained from the $(\sqrt{3}\times\sqrt{3})R30°$ surface is the same as that after 4 min of Sn deposition, which is only a little over one-half of the Sn coverage at the break point (7 min). These observations suggest that the ''monolayer Sn film'' is composed of $\frac{2}{3}$ Sn and $\frac{1}{3}$ Rh atoms and thus is intermixed. This is not an important point for any of our conclusions in this paper.

The study of Sn/Rh(111) allows us to further elucidate the correspondence between buckling distance and lattice constant mismatch.[5] The origin of the Sn buckling has been attributed to the larger Sn atomic radius compared to that of the substrate atoms. As a result, buckling is expected to relieve the strain due to incorporation of Sn into the first layer. The measured buckling was found to be linearly related to the substrate lattice constant on Sn/Pt(111), Sn/Ni(111), and Sn/Cu(111).[5] With our present data extending these previous results, the plot of the measured d_p versus the substrate lattice constant is shown in Fig. 16, where the straight line is obtained by least-squares fitting. The present data point fits a straight line exceptionally well. Indeed, this remarkable agreement indicates the strong relationship between buckling distance and lattice mismatch. We point out that identical buckling distances have been found on both (111) and (100) faces for Sn/Ni (Ref. 6) and Sn/Pt (Ref. 7) systems. These results seem to reveal a very local nature for the Sn-metal bonding in these systems and provide a challenge to devise a successful theory to explain this bonding.

The small core-level shifts for the Rh-Sn and Pt-Sn alloy surfaces in XPS suggest that alloying does not cause a major electronic redistribution. From the electronic configuration of metallic tin it may be surmised that due to a completely filled $4d$ band and unoccupied levels in the $4p$ band, the latter contribute to bonding interactions in the bimetallic Sn/

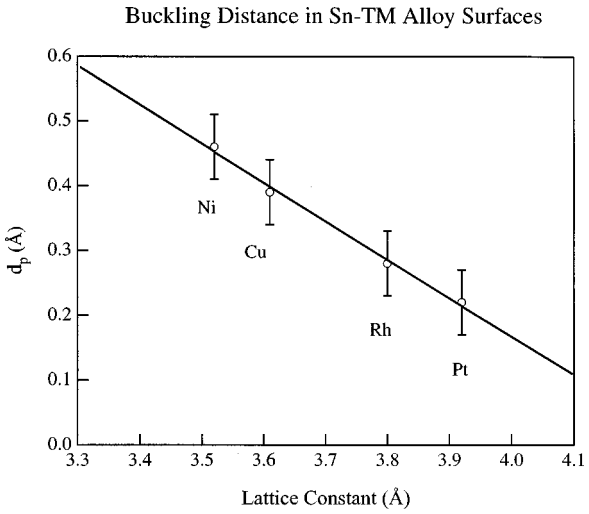

FIG. 16. A linear correlation exists between the Sn buckling distance d_p and the lattice constants of late-transition-metal fcc(111) substrates. The data point for Rh(111) was obtained in this study and the other points are from Ref. 5.

Rh(111) and Sn/Pt(111) alloy surfaces rather than any d-d bonding interactions. The valence-band shift to lower binding energy suggests that Rh $4d$ electrons and Pt $5d$ electrons are involved in the bimetallic bond on alloying, undergoing a bonding energy shift to higher binding energies. Sn is more electronegative than Rh (1.72 versus 1.45) and so electron density should be polarized toward Sn and it is easy to justify a small negative-binding-energy shift for the Sn core levels. The shifts to lower binding energy for the Rh core levels are not simple to explain. Of course it has been known for a long time that binding-energy shifts in intermetallic compounds do not simply provide the amount (or even the sign) of charge transfer in such systems.[21] Thus bonding-induced rehybridization and final-state effects play a role in the observed shifts.

Alloying Rh with Sn shifts the CO desorption temperature down by about 70 K, from 483 to 410 K. This can be compared to a shift of about 60 K, from 450 to 390 K, for the analogous $\sqrt{3}$-Sn/Pt(111) surface alloy.[22] A decrease in the CO chemisorption bond strength upon alloying is consistent with the binding-energy shifts in the valence bands for the two alloy systems. Weakening of the CO bond to the surface is expected, within the Blyholder model for CO coordination, with the localization of transition-metal valence-band d electrons to the bimetallic bond. In these alloys, rehybridization due to the bimetallic bond affecting the Rh $5s$ and/or Rh $5p$ orbitals, much like the $d\rightarrow s,p$ rehybridization that occurs in Zn/Pt(111), Cu/Pt(111), and Ag/Pt(111) systems,[23,24] also affects CO bonding. More work is needed on the $(\sqrt{3}\times\sqrt{3})$-Sn/Rh(111) system to fully understand the electronic redistribution and charge transfer upon alloying.

TPD results point to CO bonded to the $\sqrt{3}$-Sn/Rh(111) alloy surface primarily through atop sites. This can be compared to CO adsorption results on $\sqrt{3}$-Sn/Ni(111) and $\sqrt{3}$-Sn/Pt(111) alloy surfaces. CO almost does not adsorb on $\sqrt{3}$-Sn/Ni(111) surfaces at 120 K, with only about 4% of the coverage on Ni(111), occupying atop sites and desorbing at 250 K.[25] However, CO adsorption on $\sqrt{3}$-Sn/Pt(111) alloy is more nearly like that reported here for Rh-Sn, with a de-

creased CO adsorption energy, but with very little change in the saturation CO coverage or site distribution between atop and bridging sites compared to Pt(111).[22] One factor that we have previously suggested as important in these comparisons is the magnitude of the Sn–transition-metal (TM) buckling.[25] More systematic studies on related systems should help to illuminate the importance of this effect compared to the other changes occurring in the series, primarily in the transition-metal electronic structure and TM-Sn bonding interactions. Recently, Lee *et al.*[26] have also studied the Sn/Pd(111) system, finding that both (2×2) and $(\sqrt{3}\times\sqrt{3})R30°$-Sn/Pd(111) alloys can be formed. They report Pd core-level shifts that are larger than those reported above, arriving at these shifts by including the surface core-level shift. The CO adsorption energy and the saturation coverage are reduced upon alloying Sn with Pd.

V. CONCLUSION

We have studied in detail the structure of the $(\sqrt{3}\times\sqrt{3})R30°$-Sn/Rh(111) surface by using principally the ALISS and XPD techniques. It was shown that this surface is characterized by an alloy phase with a composition of $\frac{1}{3}$ ML of Sn and $\frac{2}{3}$ ML of Rh. Subsurface Sn atoms can be greatly reduced in concentration by annealing to high temperatures and a 2D alloy phase can be prepared. Sn atoms that occupy subsurface sites are in registry with Rh atoms in the bulk crystal positions. The observed buckling distance of 0.29 ± 0.05 Å is consistent with Sn behavior in other Sn-metal systems, that of outward buckling of Sn from the surface plane to relieve the strain due to lattice mismatch. This alloy phase is very stable thermally and thus provides an ideal surface on which to study chemistry. Further, we have examined the growth of films due to deposition of Sn on Rh(111) at room temperature. Pure Sn clustering growth is excluded as a possible mechanism and an alloy is formed at room temperature. It is likely that these films grow by a combination of intermixed alloy followed by 3D island growth. Finally, through a combination of XPS and CO TPD studies we have characterized some aspects of the electronic structure in the alloy. CO adsorption is more strongly affected on Rh-Sn than on Pt-Sn compared to the pure transition metals and this correlates well with the XPS results that show a stronger interaction between Rh and Sn than Pt and Sn in forming the bimetallic bond.

ACKNOWLEDGMENTS

We thank Professor M. T. Paffett for providing us with details of his work regarding the Sn-Rh(111) surface as well as lending us the Rh(111) crystal. Thanks are also due to Professor Richard Lambert for providing copies of his papers on Sn-Pd(111) surfaces prior to publication. This work was supported by the U.S. Department of Energy, Basic Energy Sciences, Chemical Sciences Division. Equipment support was provided by the Analytical and Surface Chemistry Program in the Division of Chemistry, National Science Foundation.

[1] K. Tomishige, K. Asakura, and Y. Iwasawa, J. Catal. **157**, 472 (1995).
[2] H. Niehus, W. Heiland, and E. Taglauer, Surf. Sci. Rep. **17**, 213 (1993).
[3] S. H. Overbury, D. R. Mullins, M. T. Paffett, and B. E. Koel, Surf. Sci. **254**, 45 (1991).
[4] Y.-S. Ku and S. H. Overbury, Surf. Sci. **273**, 341 (1992).
[5] S. H. Overbury and Y.-S. Ku, Phys. Rev. B **46**, 7868 (1992).
[6] Y. D. Li, L. Q. Jiang, and B. E. Koel, Phys. Rev. B **49**, 2813 (1994).
[7] Y. D. Li and B. E. Koel, Surf. Sci. **330**, 193 (1995).
[8] C. S. Fadley, M. A. Van Hove, Z. Hussain, and A. P. Kaduwela, J. Electron Spectrosc. Relat. Phenom. **75**, 273 (1995), and references therein.
[9] W. F. Egelhoff, Jr., in *Ultrathin Magnetic Structures I: An Introduction to Electronic, Magnetic, and Structural Properties*, edited by J. A. C. Bland and B. Heinrich (Springer-Verlag, Berlin, 1994), p. 220.
[10] M. Galeotti, A. Atrei, U. Bardi, G. Rovida, and M. Torrini, Surf. Sci. **313**, 349 (1994).
[11] A. Sellidj and B. E. Koel, J. Phys. Chem. **97**, 10 076 (1993).
[12] T. N. Taylor, M. A. Hoffbauer, C. J. Maggiore, and J. G. Beery, J. Vac. Sci. Technol. A **5**, 1625 (1988).
[13] M. T. Paffett (private communication).
[14] S. H. Overbury and D. R. Huntley, Phys. Rev. B **32**, 6278 (1985).
[15] E. Janin, M. Bjorkqvist, T. M. Grehk, M. Gothelid, C.-M. Pradier, U. O. Karlsson, and A. Rosengren, Appl. Surf. Sci. **99**, 371 (1996).
[16] P. A. Redhead, Vacuum **12**, 203 (1962).
[17] D. G. Castner, B. A. Sexton, and G. A. Somorjai, Surf. Sci. **71**, 519 (1978).
[18] P. A. Thiel, E. D. Williams, J. T. Yates, Jr., and W. H. Weinberg, Surf. Sci. **84**, 54 (1979).
[19] L. H. Dubois and G. A. Somorjai, Surf. Sci. **91**, 514 (1980).
[20] W. F. Egelhoff, Jr., *DOE Workshop on Surface Diffusion and the Growth of Materials*, edited by P. J. Feibelman, G. L. Kellogg, and T. A. Michalske (Sandia National Laboratory, Albuquerque, NM, 1992), Vol. 1, p. 50.
[21] G. K. Wertheim, D. N. E. Buchanan, and J. H. Vermick, Phys. Rev. B **40**, 5319 (1988).
[22] M. T. Paffett, S. C. Gebhard, R. G. Windham, and B. E. Koel, J. Phys. Chem. **94**, 6831 (1990).
[23] J. A. Rodriguez and M. J. Kuhn, J. Phys. Chem. **98**, 11 251 (1994).
[24] J. A. Rodriguez and M. J. Kuhn, J. Chem. Phys. **102**, 4279 (1995).
[25] C. Xu and B. E. Koel, Surf. Sci. **327**, 38 (1995).
[26] A. F. Lee, C. J. Baddley, M. S. Tikhov, and R. M. Lambert, Surf. Sci. **373**, 195 (1997).